IEEE Access
Multidisciplinary | Rapid Review | Open Access Journal

Received October 4, 2021, accepted October 19, 2021, date of publication October 25, 2021,
date of current version November 17, 2021.

Digital Object Identifier 10.1109/ACCESS.2021.3122575

A Class of Lightweight Spherical-Axicon Dielectric Lenses for High Gain Wideband Antennas

RENATO CICCHETTI[1], (Senior Member, IEEE), VALENTINA CICCHETTI[1], ANTONIO FARAONE[2], (Senior Member, IEEE), AND ORLANDINO TESTA[1]

[1]Department of Information Engineering, Electronics and Telecommunications, University of Rome "La Sapienza," 00184 Rome, Italy
[2]Motorola Solutions, Inc., Fort Lauderdale, FL 33322, USA

Corresponding author: Renato Cicchetti (renato.cicchetti@uniroma1.it)

ABSTRACT A class of lightweight spherical-axicon-like dielectric lenses suitable for enhancing broadband antennas performances is presented. The proposed lenses, sized according to a reference massive lens, are formed by thin dielectric sheets spaced equiangularly on the azimuth plane (petal-shaped lens), or regularly orthogonally arranged along the lens axis (disks-shaped lens), thus yielding construction simplicity and significant weight reduction. While petal-shaped dielectric lenses are shown to yield mild gain increase, lenses made by thin dielectric disks, orthogonally periodically arranged along the lens optical axis, offer performances much closer to those achieved by comparable massive refractive spherical-axicon dielectric lenses. The time-domain and the focusing characteristics of the proposed lenses are investigated. Then, a Floquet's mode-based model is proposed to describe the stop-band characteristics of stacked-disk lenses, illustrating the mechanism underpinning their sudden performance degradation observed at the stop-band onset frequency. Full-wave analyses, based on a locally conformal finite integration technique (FIT), implemented in CST Studio Suite™ and validated by measurements or highly accurate FEM simulations, illustrate the excellent characteristics of the proposed lenses to operate with narrowband as well as ultra-wideband (UWB) waveforms.

INDEX TERMS Dielectric resonator antennas (DRA), high gain wideband antenna, petal-shaped dielectric lens, spherical-axicon dielectric lens, stacked-disk dielectric lens, traveling-wave antennas, Vivaldi antenna, wideband dielectric lens.

I. INTRODUCTION

Mobile and satellite communication systems [1]–[3] weather radars [4], RF sensing [5], [6], and through-the-wall imaging (TWI) systems [7]–[9], as well as compact antenna test ranges [10] can benefit from the use of antennas featuring performance-enhancing dielectric lenses. These lenses can be designed to increase gain and front-to-back ratio, equalizing these parameters within the antenna operating band, thus achieving compact size and light weight of the resulting radiating system. While lenses for optical applications [11], for millimeter wave [12]–[15] or for THz frequencies [1], [16], are generally characterized by light weights, those used in radiating systems designed to operate in the lower end of the microwaves band may exhibit significant weight [1], [14], as it happens in the case of weather radar or through-the-wall imaging systems [17]. Furthermore, air and space borne radio systems typically require wideband radiating systems characterized by a small footprint, cost and weight. Unlike optics applications, microwave lens dimensions may range up to a few operating wavelengths so the lens behavior is quasi-optical and cannot be analyzed using ray optics [14], [18]. Therefore, rigorous full-wave techniques become necessary in the lens antenna analysis and design.

Canonical lens shapes adopted in elliptical [15], spherical [19], [20], hemispherical or extended hemispherical lenses [21], [22] as well as gradient-refractive-index (GRIN) [23], [24], and custom-shaped [25], [26] dielectric lenses have been widely employed in the synthesis of complex field profiles [14]. While lenses having canonical shapes are moderately expensive and readily manufacturable, GRIN and custom-shaped dielectric lenses are not only computationally onerous to design but their realization may be particularly complex and therefore expensive. Recently, a class

The associate editor coordinating the review of this manuscript and approving it for publication was Bilal Khawaja.

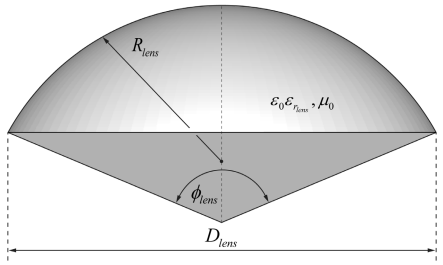

FIGURE 1. Spherical-axicon dielectric lens formed by a spherical cap (plano-convex lens) and a dielectric cone. The geometrical and electrical parameters that identify the lens are shown in the figure.

of dielectric lenses suitable to be integrated into broadband antennas was proposed, which combines the advantages offered by the plano-convex lens [21], [27] with those of an axicon lens [28]. Such "spherical-axicon" dielectric lenses [17], formed by the union of a spherical cap and a dielectric cone, feature the interesting property of focusing RF energy near the lens vertex across wide operating bandwidths, exhibiting small electrical size. In turn, this feature leads to compact, broadband radiating structures since RF energy can be focused near the lens excitation system [29], or near the radiating aperture of traveling wave antennas [17]. Besides being cost effective, the lens design is rather efficient since only three geometric parameters (the spherical cap radius R_{lens} and diameter D_{lens}, and the cone opening angle ϕ_{lens}) and the lens relative dielectric permittivity $\varepsilon_{r_{lens}}$ define the structure. Indeed, the lens size and weight could be moderately large in the lower microwave range, especially when high antenna gain is required. Therefore, techniques leading to lighter lens and lower cost designs are desirable.

In this work, two alternative approaches, featuring composite lens structures, are investigated using full-wave analysis (CST Studio Suite^{TM}), which lead to dielectric lens designs with similar performances of massive lenses, but yielding lower weight and cost. The corresponding performances are benchmarked against known antenna structures featuring massive spherical-axicon dielectric lenses [17], [29].

II. LIGHTWEIGHT SPHERICAL-AXICON-LIKE DIELECTRIC LENSES

Massive spherical-axicon dielectric lenses (see Fig. 1) have been shown to improve the radiative performances of compact broadband antennas operating with time-harmonic or impulsive signals [17], [29].

In air and space-borne applications, strict limits on the radiating system bare weight may be imposed at the design stage. In this section, we present two composite lens designs (dubbed "petal-shaped" and "stacked-disk", respectively) featuring low weight and manufacturing simplicity, which are shown to approach the electromagnetic behavior of a benchmark massive spherical-axicon lens having the same geometrical envelope. In particular, two benchmark embodiments, featuring broadband operation, high gain and high front-to-back ratio are considered: a first one based on the so-called "Mushroom-Shaped Dielectric Resonator Antenna" [29], and a second one based on the so-called "Wideband Lens Vivaldi Antenna" [17]. In this work, these two antenna systems will be considered with and without massive or lightweight lenses. The studied lens antennas were characterized using the adaptive-mesh FIT technique, after validating selected results against the corresponding finite element method (FEM) solutions of identical solid models, via the corresponding solver available in CST Studio Suite^{TM}.

A. PETAL-SHAPED DIELECTRIC LENS

Two distinct thin petal-shaped dielectric-slab lenses, designed with the same geometrical envelope of the benchmark massive spherical-axicon dielectric lens (see Fig. 2), are studied varying the slab permittivity and the number of petals forming the lens, across the operating bands of the benchmark antennas, each capable to sustain linear (LP) and circular polarization (CP).

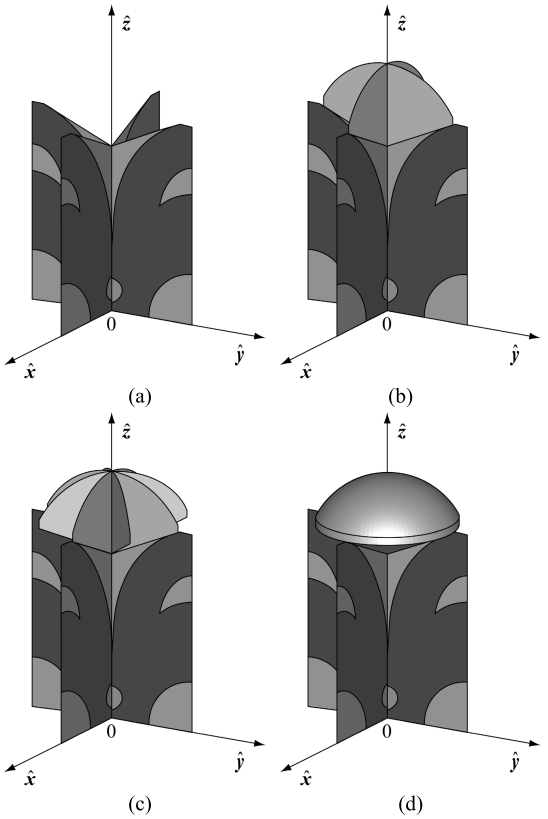

FIGURE 2. Vivaldi antenna-based embodiments without lens (a); equipped with 4-petal lens (b); and with 8-petal lens (c); fitting the geometrical envelope of the massive lens (d). The radiating structure is formed by the cross-assembly of two Vivaldi antennas, so as to excite linear and circular polarizations [17]. The outer edge corrugations appearing on the Vivaldi arms help increase gain and reduce the lower operational frequency bound.

The main characteristics of the benchmark antennas are reported in Table 1, while the geometrical parameters

describing the respective massive spherical-axicon dielectric lenses are listed in Table 2.

The massive lens implemented in the Vivaldi antenna (see Fig. 2d) yields 16 dBi peak realized gain when the antenna operates in linear or circular polarization.

Two different petal-shaped dielectric-slab lenses, featuring four and eight equiangular petals, respectively, fitting within the massive lens envelope are shown in Figs. 2b and 2c. The lens slab thickness was chosen equal to the Vivaldi antenna substrate (0.813 *mm*), while several commercially available materials, having relative dielectric permittivity $\varepsilon_r = 2.1$ (Teflon), or $\varepsilon_r = 6.15$ and $\varepsilon_r = 10.2$ (Rogers substrates), were considered. Table 3 reports the corresponding peak gains, weights and effective volumetric dielectric permittivities (computed as the mean relative to the benchmark massive antenna volume), as well as a quite revealing figure of merit given by the ratio of the dBi antenna peak gain and the lens weight. Figs. 3 and 4 report the frequency behaviors of the Total Active Reflection Coefficient (TARC) [30] and the antenna right-hand circular polarization (RHCP) realized gain, for petal-shaped lenses with the various considered substrates, as well as the reference behaviors with and without the benchmark massive lens. The following expression

$$\Gamma_{TARC} = \sqrt{1 - \frac{\boldsymbol{a}^+ \cdot \underline{\boldsymbol{Q}}_R \cdot \boldsymbol{a}}{\boldsymbol{a}^+ \cdot \boldsymbol{a}}}, \tag{1}$$

where "+" denotes the Hermitian transpose operator, while $\boldsymbol{a}$ is the incident wave vector exciting the two-port antenna and $\underline{\boldsymbol{Q}}_R$ its dissipation matrix [31], was used to compute the TARC. Minor perturbations of the TARC occur in the antenna operating band (0.65-6 GHz), while the RHCP gain tends to increase with the number of dielectric-slab petals and their relative permittivities. However, for the 8-petal lens such a trend ceases as the frequency approaches the upper bound of the operating range, where a steep gain reduction occurs. Such an effect could be related to excessive effective dielectric permittivity radial gradient, when employing more than four petals. Similar trends are observed when operating in linear polarization. Hence, for the sake of brevity, only the case of the antenna operating in circular polarization is reported in the following.

The cross polarization level as the number of dielectric petals increases, across the operating band of the antenna working in RHCP, is helpful to quantify the field purity. For the sake of brevity, Table 4 shows the desired RHCP and undesired LHCP gain values for the 8-petal lens antenna with relative permittivity $\varepsilon_r = 10.2$ and for the benchmark massive one ($\varepsilon_r = 2.1$).

Both the petal-shaped and the benchmark massive lens yield higher RHCP gain and lower LHCP gain than in the absence of any lens, with the latter presenting better polarization purity overall.

Impulsive signals may be employed for UWB communications [32] or for through-the-wall radars imaging and through-the building sensing systems [33]. As both

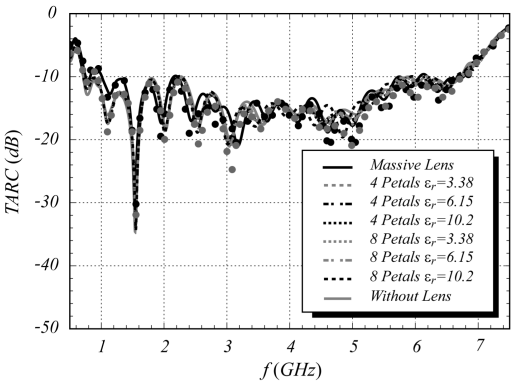

FIGURE 3. TARC versus frequency for the RHCP Vivaldi-based antenna equipped with 4- and 8-petal dielectric lenses featuring similar operating bands. Black and grey dots represent reference FEM results for the massive and 8-petal ($\varepsilon_r = 6.15$) lens antennas, respectively.

TABLE 1. Antennas characteristics.

	Vivaldi Antenna [17]	*Mushroom DRA* [29]
Bandwidth	0.650-6 GHz	4.6-9.1 GHz
FBW	160%	65%
Peak Gain LP	16 dBi	16 dBi
Peak Gain CP	16 dBi	16 dBi

TABLE 2. Massive spherical-axicon dielectric lens parameters.

	Vivaldi Antenna [17]	*Mushroom DRA* [29]
R_{lens}	100.93*mm*	32*mm*
D_{lens}	177.78*mm*	60.87*mm*
ϕ_{lens}	133.92°	144°
$\varepsilon_{r_{lens}}$	2.1	4

applications are of great interest, as in [17] the antenna was excited at the first antenna port (with the second port closed on a matched load) with an incident wave having a monocycle waveform obtained from the first derivative of the Gaussian pulse

$$a_1(t) = -\sqrt{e}\frac{t - t_0}{\sigma} e^{-\frac{(t-t_0)^2}{2\sigma^2}} \tag{2}$$

with $\sigma = 0.075$ *ns* and $t_0 = 5\sigma$. With these parameters, the $-3dB$ bandwidth extends between about 1 *GHz* to about 3.5 *GHz*. The monocycle is preferred over other waveforms to detect targets buried or placed beyond a wall [34]. The time domain antenna responses, computed at a distance of 1 *m* from the antenna in the *xz*-plane for a 8-petal dielectric lens as the petal permittivity varies, benchmarked against the corresponding massive lens response, are shown in Fig. 5.

As shown, the ringing levels remain well bounded and similar to that of the benchmark lens. The similarities are also confirmed by the frequency behavior of the relative group

TABLE 3. Characteristics of the Vivaldi-based petal-shaped lens antenna.

	Lens Relative Dielectric Permittivity	Lens Effective Dielectric Permittivity	Peak Gain (dBi)	Lens Weight (g)	$\frac{\text{Max Gain}}{\text{Weight}}\left(\frac{\text{dBi}}{\text{g}}\right)$
4-Petal Lens	3.38	1.04	10.7	34.55	0.310
	6.15	1.08	11.0	49.99	0.221
	10.2	1.14	11.4	53.84	0.212
8-Petal Lens	3.38	1.07	11.0	69.75	0.158
	6.15	1.15	12.1	99.81	0.121
	10.2	1.27	11.6	107.5	0.108
Massive Lens	2.1	2.10	15.7	2623	0.006

TABLE 4. Frequency behavior of the antenna realized gain (RHCP and LHCP), for the RHCP Vivaldi-based antenna.

f (GHz)	RHCP Gain Without Lens (dBi)	LHCP Gain Without Lens (dBi)	RHCP Gain 8-Petal Lens ($\varepsilon_r = 10.2$) (dBi)	LHCP Gain 8-Petal Lens ($\varepsilon_r = 10.2$) (dBi)	RHCP Gain Massive Lens ($\varepsilon_r = 2.1$) (dBi)	LHCP Gain Massive Lens ($\varepsilon_r = 2.1$) (dBi)
1	6.44	-5.35	6.60	-5.86	7.31	-8.13
2	8.70	-6.60	9.62	-8.32	11.7	-11.02
3	9.06	-5.78	11.2	-3.48	14.0	-3.28
4	8.49	-0.84	11.5	1.85	15.0	2.32
5	8.49	-3.15	11.5	-1.08	15.7	2.42
6	8.88	-3.50	10.1	-1.92	15.7	7.47

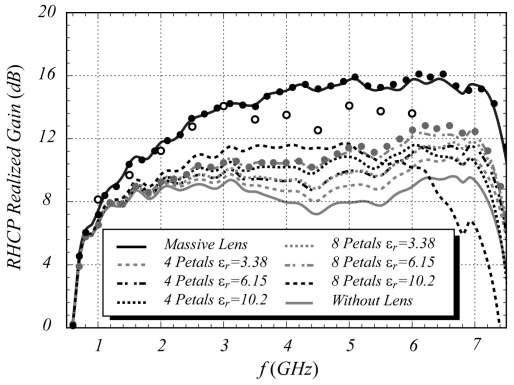

FIGURE 4. Peak realized antenna gain versus frequency for the RHCP Vivaldi-based antenna. Empty circles trace the experimental measurements reported in [17]. Black and grey dots represent reference FEM results for the massive and 8-petal ($\varepsilon_r = 6.15$) lens antennas, respectively. A gain drop is observed around 6 GHz for the antenna equipped with 8-petal dielectric lens having relative permittivity $\varepsilon_r = 10.2$. Best gain performances are obtained using the massive lens. Excellent agreement between FIT and FEM results is observed.

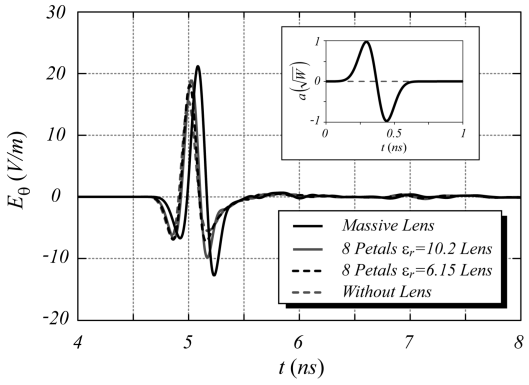

FIGURE 5. Time-domain electric field response in the xz-plane ($\theta = 0°$) when the antenna is matched at port 2 and excited at port 1 by a Gaussian monocycle incident waveform with maximum amplitude $1\sqrt{W}$. Higher values of the radiated signal are obtained using a massive lens even tough good performances are obtained using an 8-petal dielectric lenses with relative dielectric permittivity 6.15 and 10.2. Little ringing is observed in all antenna responses.

delay computed along the antenna boresight (see Fig. 6). Hence, petal-shaped dielectric lenses represents a meaningful compromise when it is necessary to choose whether to use no lens or a massive lens, as they exhibit good performances in both frequency and time domains, without excessively increasing the antenna complexity, cost and weight.

A parallel investigation, carried out by integrating similar petal-shaped lenses, albeit with permittivity $\varepsilon_r = 4$,

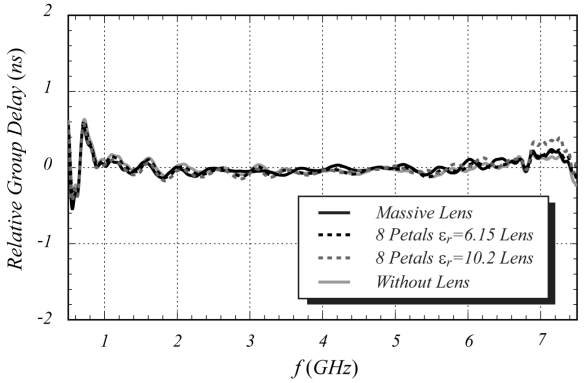

FIGURE 6. Frequency behavior of the relative group delay as the dielectric permittivity of the 8-petal dielectric lens varies. An excellent behavior is exhibited by the three dielectric lenses. Similar results are obtained when the petal number is lower.

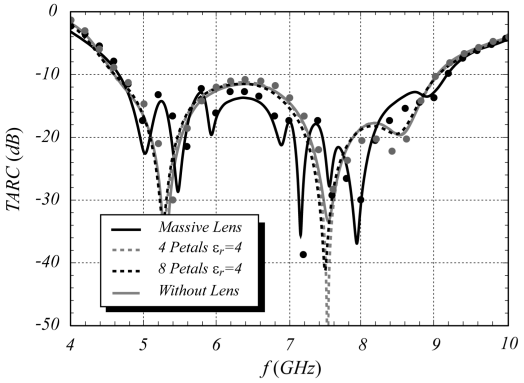

FIGURE 7. TARC versus frequency for the DRA-based antenna working in right-hand circular polarization (RHCP). The antenna operating band does not change significantly, with respect to the antenna equipped with the massive lens, as the number of petals forming the lightweight dielectric lens varies. Black and grey dots represent reference FEM results for the massive and 4-petal ($\varepsilon_r = 4$) lens antennas, respectively.

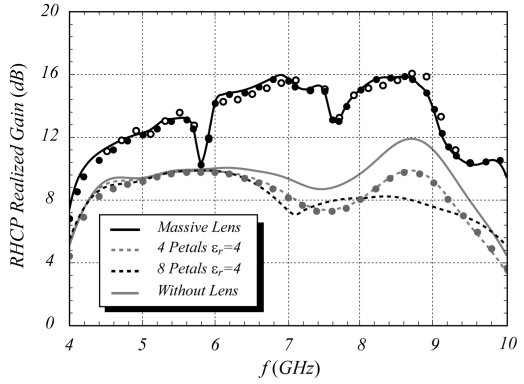

FIGURE 8. Peak realized gain versus frequency for the DRA-based antenna working in right-hand circular polarization (RHCP). Empty circles trace the measurements from [29]. Black and grey dots represent reference FEM results for the massive and 4-petal ($\varepsilon_r = 4$) lens antennas, respectively. Note the poor performance using petal-shaped dielectric lenses; gain may only be improved using at least 40 petals. Excellent agreement between FIT and FEM results is observed.

over a cylindrical DRA operating in RHCP [29] is briefly presented. While a weak impact on the TARC upon increasing the number of petals was observed (see Fig. 7), the RHCP gain was significantly degraded compared with the benchmark massive lens (see Fig. 8). Specifically, when the DRA-based system is equipped with less than about 20 petals, the observed performances did not exceed those without lens, whereas an increase in the realized gain can still be observed (up to 3 dB) when the DRA-based system is equipped with a 40-petal lens, even though such an improvement only occurs between 4 and 8.5 GHz. This particular behavior, probably linked to a radial dependence of the lens effective dielectric permittivity, has a weak impact on the Vivaldi-based antenna, while it becomes significant in the DRA-based antenna. Furthermore, it was observed that the gain does not increase monotonically with the number of petal elements.

B. STACKED-DISK DIELECTRIC LENS

A novel dielectric lens, consisting of thin, parallel dielectric disks periodically arranged along the boresight axis following the envelope of the benchmark massive spherical-axicon dielectric lens (see Fig. 9), was investigated. The slabs are held together by means of a thin Plexiglas cylinder ($\varepsilon_r = 3.6$) having diameter 4 *mm*.

A one-dimensional Floquet's mode-based model was developed for a rough estimate of the first stop-band frequency and of the effective relative dielectric permittivity $\varepsilon_{r_{eff}}$ for a TEM wave propagating across the periodic structure featuring an elemental cell of length l, consisting of an air gap and a thin dielectric slab of thickness t and relative dielectric permittivity ε_r. Using the ABCD transmission matrix of the aforementioned unit cell [35] and evaluating its eigenvalues $\lambda_\pm$, the following equation is obtained

$$\lambda_\pm = \cos\left[\beta_0 (l-t)\right]\cos\left(\beta_d t\right) - \frac{\eta_0^2+\eta_d^2}{2\,\eta_0\,\eta_d}\sin\left[\beta_0 (l-t)\right] \times \sin\left(\beta_d t\right) \pm \left\{\left[\cos\left[\beta_0 (l-t)\right]\cos\left(\beta_d t\right) - \frac{\eta_0^2+\eta_d^2}{2\,\eta_0\,\eta_d}\sin\left[\beta_0 (l-t)\right]\sin\left(\beta_d t\right)\right]^2 - 1\right\}^{\frac{1}{2}} \quad (3)$$

where η_0, η_d, and β_0, β_d are the characteristic impedance and the propagation constant in free space and in the dielectric slab, respectively. The frequency ranges in which propagation may occur, are derived by enforcing the radicand of (3) to be negative. Further developing (3) under the thin slab hypothesis yields the approximate dispersion equation

$$\cot\left[\beta_0 (l-t)\right] \geq -\frac{4-\beta_0^2\,(1+\varepsilon_r)^2\,t^2}{4\beta_0\,(1+\varepsilon_r)\,t} \quad (4)$$

whose solution reveals the propagation and stop-band characteristics of the periodic structure. An approximate solution for the first stop-band frequency f_c can be obtained by expanding the first member of (4) around its first zero, and the second member around the zero of the numerator, yielding

$$f_c \cong \frac{c}{2\pi}\,\frac{2+\pi}{2\,(l-t)+(1+\varepsilon_r)\,t}, \quad (5)$$

where c is the free-space speed of light.

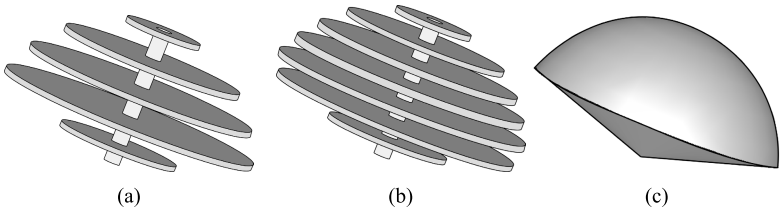

FIGURE 9. Geometrical models of the (a) 5-disk; (b) 7-disk dielectric lens; and (c) benchmark massive dielectric lens. The disks are held together by means of a thin dielectric Plexiglas cylinder ($\varepsilon_r = 3.6$).

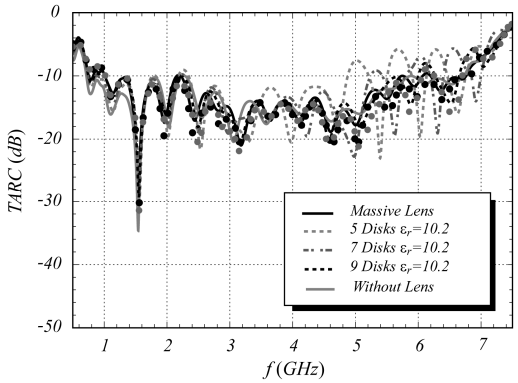

FIGURE 10. TARC versus frequency for the RHCP Vivaldi-based antenna. Best performance are obtained with the 9-disk lens featuring only a limited reduction of the antenna operating band while reducing the mass six-fold. Black and grey dots represent reference FEM results for the massive and 9-disk ($\varepsilon_r = 10.2$) lens antennas, respectively.

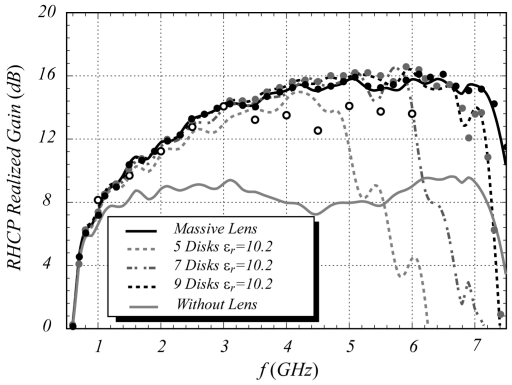

FIGURE 11. Peak realized gain versus frequency for the RHCP Vivaldi-based antenna. Empty circles trace the experimental measurements reported in [17]. Black and grey dots represent reference FEM results for the massive and 9-disk ($\varepsilon_r = 10.2$) lens antennas, respectively. Best performances are achieved with the 9-disk lens featuring gain similar to the massive lens up to about 6.6 GHz. The onset of the stop bands for the stacked-disk lenses is clearly reflected in the corresponding gain drops. Excellent agreement between FIT and FEM results is observed.

The effective relative dielectric permittivity $\varepsilon_{r_{eff}}$ is then evaluated from the periodic structure equivalent transmission line model. By expanding this parameter with respect to the slab thickness t up to the second order, the following approximation, which is valid for $f < f_c$, is obtained

$$\varepsilon_{r_{eff}} \cong 1 + \frac{(\varepsilon_r - 1)\, t}{l} + \frac{(\varepsilon_r - 1)^2 \left[1 - \beta_0 l \cot \beta_0 l\right]}{4} \left(\frac{t}{l}\right)^2 \tag{6}$$

which shows a weak increase of $\varepsilon_{r_{eff}}$ with frequency. Equations (5)-(6) will be employed to derive the lens design guidelines illustrated in the following.

Tables 5 and 6 show the weights, the length of the unit cell l, the values of the effective dielectric permittivity, computed using the quasi-static term in (6) for $t = 1.28$ *mm*, the onset frequency of the first stop band, from (5), of the lenses, as well as the peak gains attained by the Vivaldi-based and the DRA-based antennas.

Although several lens dielectric materials have been considered, only the performance for disks with $t = 1.28$ *mm* and $\varepsilon_r = 10.2$ are reported for the sake of brevity.

The TARC frequency behaviors for the RHCP Vivaldi-based antenna equipped with an increasing number of disks are shown in Fig. 10, while the respective RHCP gain behaviors are reported in Fig. 11. The 7-disk lens has an impedance matching and gain similar to that of the massive lens up to about 5.2 GHz, while the 9-disk lens, whose $\varepsilon_{r_{eff}} = 2.05$ (see Table 5), exhibits performance similar to the massive lens up to about 6.6 GHz (see Fig. 11). Such behavior suggest that better performances are generally attainable when the stacked lens effective permittivity approaches the massive lens permittivity, as further discussed in the design guidelines section.

The behavior of the (unwanted) LHCP gain is reported in Table 7, while the antenna response to the monocycle pulse (2) is shown in Fig. 12. Also in this case extremely low ringing levels are observed. The frequency behavior of the relative group delay is shown in Fig. 13, showing increasing levels above 5.3 GHz for the structure equipped with the 7-disk lens, while the increase occurs outside the antenna operating band for the 9-disk lens. These increases are in line with the gain degradation caused by the stop band onset (see Fig. 11).

The results illustrated in the foregoing demonstrate the feasibility and the excellent performances, albeit within the respective stop band limitations, of stacked-disk lenses in terms of desired RHCP and unwanted LHCP gains (see Table 7), compared to those obtainable without lens. The results further illustrate the feasibility of achieving much

TABLE 5. Characteristics of the Vivaldi-based antenna equipped with stacked-disk lenses.

	Lens Relative Dielectric Permittivity	Lens Effective Dielectric Permittivity	First Stop-Band Onset Frequency (GHz)	Peak Gain (dBi)	Lens Weight (g)	$\frac{\text{Max Gain}}{\text{Weight}}$ (dBi/g)
3-Disk Lens $l = 3.36cm$	2.1	1.04	3.6	9.8	108	0.091
	6.15	1.96	3.3	11.3	127	0.089
	10.2	1.35	3.1	12.1	137	0.088
5-Disk Lens $l = 2.02cm$	2.1	1.07	5.9	10.0	173	0.058
	6.15	1.33	5.2	13.0	204	0.064
	10.2	1.58	4.7	14.9	220	0.068
7-Disk Lens $l = 1.44cm$	2.1	1.10	8.1	10.3	254	0.041
	6.15	1.46	6.9	14.1	300	0.047
	10.2	1.82	6.1	16.4	323	0.051
9-Disk Lens $l = 1.12cm$	2.1	1.13	10.3	10.6	326	0.033
	6.15	1.59	8.5	15.0	386	0.039
	10.2	2.05	7.2	16.3	415	0.039
Massive Lens	2.1	2.10	-	15.7	2623	0.006

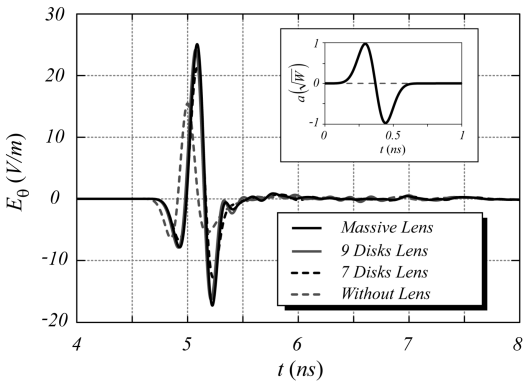

FIGURE 12. Time-domain behavior of the co-polarized component of the electric field radiated by the Vivaldi-based antenna equipped with a stacked 7- and 9-disk dielectric lens having relative permittivity $\varepsilon_r = 10.2$ and with a massive lens ($\varepsilon_r = 2.1$) computed at a distance of 1 *m* along the *z*-axis. The time delay introduced by the lenses is evident. The impulse signal (monocycle) used to excite the structures is also shown.

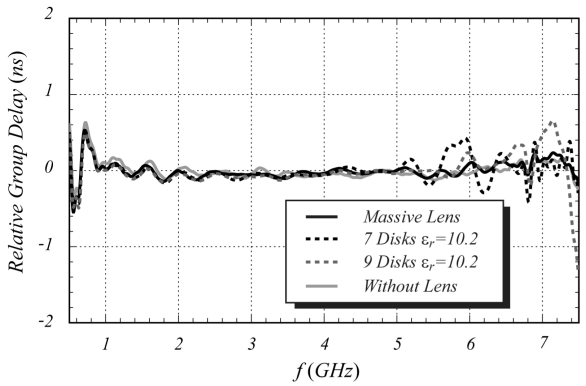

FIGURE 13. Frequency-domain behavior of the relative group delay featured by the Vivaldi-based antenna equipped with a stacked 7-disk and 9-disk dielectric lenses ($\varepsilon_r = 10.2$) and with a massive lens ($\varepsilon_r = 2.1$) computed at a distance of 1 *m* along the *z*-axis. A limited perturbation of the group delay is observed in the antenna equipped with stacked-disk lenses when the antenna works near its maximum working frequency.

lighter antenna structures approximating the performances of massive dielectric lenses.

Moving to DRA-based embodiments, the geometries of the wideband DRA-based system without lens, with 5-disk lens, and with a massive lens are shown in Fig. 14.

The TARC frequency behaviors for DRA-based antennas equipped with 5-disk and 7-disk lenses ($\varepsilon_r = 10.2$), as well as the massive spherical-axicon dielectric lens ($\varepsilon_r = 4$), are reported in Fig. 15, while the corresponding RHCP gain behaviors are shown in Fig. 16. The frequency behaviors of the desired RHCP and the unwanted LHCP gains are reported in Table 8.

Finally, the responses to an impulsive waveform related to the fifth derivative of the Gaussian pulse

$$a_1(t) = c_s \frac{t - t_0}{\sigma^6} \left[-15 + 10 \left(\frac{t - t_0}{\sigma} \right)^2 - \left(\frac{t - t_0}{\sigma} \right)^4 \right] \times e^{-\frac{(t-t_0)^2}{2\sigma^2}} \quad (7)$$

where c_s is a parameter ensuring unitary maximum amplitude and t_0 is the time corresponding to the Gaussian pulse maximum, while σ determines the signal time spread, are shown in Fig. 17. For $\sigma = 51$ *ps*, the signal frequency spectrum fits the US Federal Communications Commission emission mask

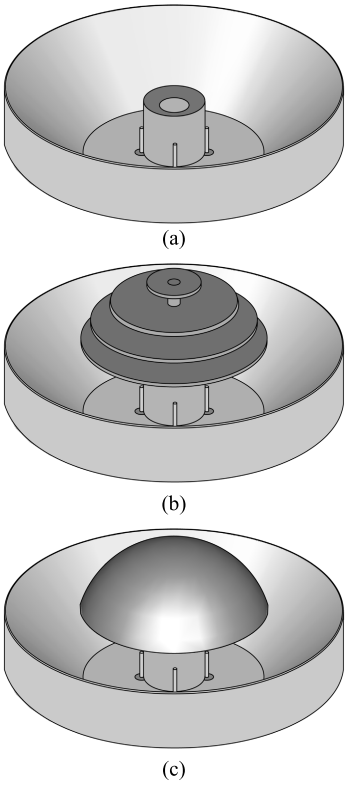

FIGURE 14. Geometrical models of the DRA-based system (a) without lens; (b) with a 5-disk lens; and (c) with massive lens. The coaxial probes next to the DR may excite linear or circular polarization, while the reflector shape is designed to increase antenna gain and front-to-back ratio.

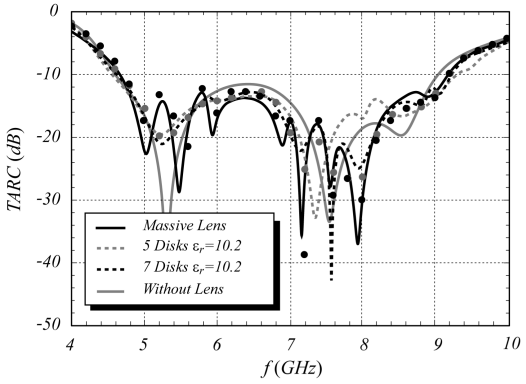

FIGURE 15. TARC versus frequency for the DRA-based antenna versus the number of dielectric disks ($\varepsilon_r = 10.2$). The operating band remains substantially unchanged with respect to the massive lens antenna ($\varepsilon_r = 4$). Black and grey dots represent reference FEM results for the massive and 7-disk ($\varepsilon_r = 10.2$) lens antennas, respectively.

for UWB indoor wireless communications in the 3–11 GHz band [32].

Unlike we saw for the petal-shaped lenses, these results illustrate that stacked-disk lenses approach the performances of the benchmark massive lens in terms of gain (see Table 8) and time-domain characteristics (see Fig. 17), and may even provide improved group delay characteristics (see Fig. 18).

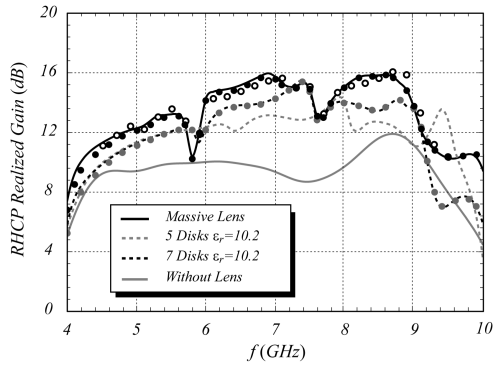

FIGURE 16. Peak realized gain versus frequency for the DRA-based RHCP antenna equipped with 5-disk and 7-disk dielectric lenses ($\varepsilon_r = 10.2$) and the massive lens ($\varepsilon_r = 4$). Empty circles trace the measurements from [29]. Black and grey dots represent reference FEM results for the massive and 7-disk ($\varepsilon_r = 10.2$) lens antennas, respectively. Both lightweight lenses yield significant gain improvements. Excellent agreement between FIT and FEM results is observed.

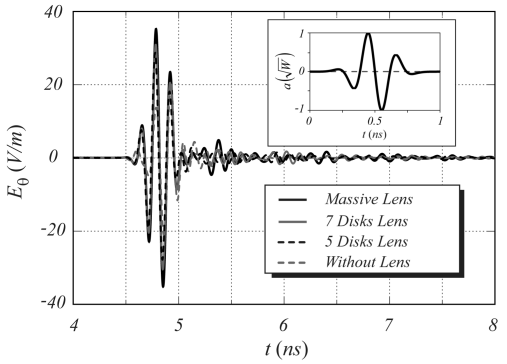

FIGURE 17. Time domain behavior of the co-polarized electric field component radiated by the DRA-based antennas, equipped with a massive lens, and with 5-disk and 7-disk dielectric lenses, at a distance of 1m along the z-axis. A slightly lower amplitude pulse and a more limited ringing level is observed in the temporal response of the antenna equipped with a 7-disk dielectric lens. The impulse signal used to excite the structures is also shown.

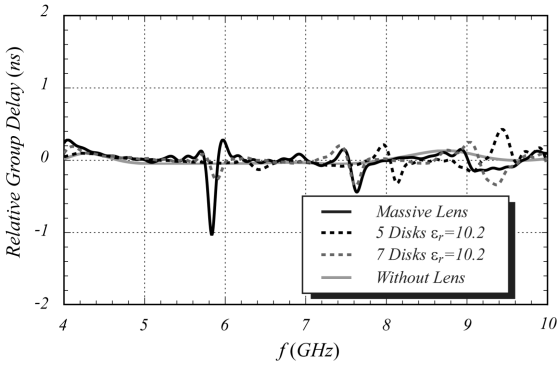

FIGURE 18. Frequency behavior of the relative group delay for the lensless DRA system, of the DRA-based antennas equipped with 5-disk and 7-disk dielectric lens ($\varepsilon_r = 10.2$) and with a massive lens ($\varepsilon_r = 4$). The resonance process taking place in the massive lens at about 5.8 GHz [29] is strongly damped in the 7-disk dielectric lens.

III. FOCUSING CHARACTERISTICS OF THE PROPOSED LENSES

Short focal-length dielectric lenses enable to compact broadband antennas when integrated close to or within antenna feeding systems (probes, slits, radiating apertures, etc.),

TABLE 6. Characteristics of the DRA-based equipped with stacked-disk lenses.

	Lens Relative Dielectric Permittivity	Lens Effective Dielectric Permittivity	First stop-band Onset Frequency (GHz)	Peak Gain (dBi)	Lens Weight (g)	$\frac{\text{Max Gain}}{\text{Weight}}$ (dBi/g)
3-Disk Lens $l = 1.37cm$	4	1.28	7.9	10.6	9.7	1.09
	6.15	1.48	7.2	11.25	12.4	0.907
	10.2	1.86	6.3	12.25	12.4	0.988
5-Disk Lens $l = 0.69cm$	4	1.55	13.9	10.94	21.8	0.502
	6.15	1.96	12.0	11.56	27.8	0.416
	10.2	2.71	9.6	14.25	27.8	0.513
7-Disk Lens $l = 0.46cm$	4	1.83	18.8	11.33	32.3	0.351
	6.15	2.43	15.5	12.75	41.1	0.310
	10.2	3.56	11.7	15.37	41.1	0.374
9-Disk Lens $l = 0.34cm$	4	2.13	23.1	11.83	42.6	0.278
	6.15	2.94	18.3	15.22	50.4	0.302
	10.2	4.46	13.2	15.02	54.3	0.277
Massive Lens	4	4.00	-	16.10	104	0.155

TABLE 7. Frequency behavior of the antenna realized gain (RHCP and LHCP), for the RHCP Vivaldi-based antenna.

f (GHz)	RHCP Gain Without Lens (dBi)	LHCP Gain Without Lens (dBi)	RHCP Gain 9-Disks Lens ($\varepsilon_r = 10.2$) (dBi)	LHCP Gain 9-Disks Lens ($\varepsilon_r = 10.2$) (dBi)	RHCP Gain Massive Lens ($\varepsilon_r = 2.1$) (dBi)	LHCP Gain Massive Lens ($\varepsilon_r = 2.1$) (dBi)
1	6.44	-5.35	7.44	-7.52	7.31	-8.13
2	8.70	-6.60	11.7	-8.43	11.7	-11.02
3	9.06	-5.78	14.1	-3.88	14.0	-3.28
4	8.49	-0.84	15.3	1.80	15.0	2.32
5	8.49	-3.15	15.9	1.28	15.7	2.42
6	8.88	-3.50	16.4	5.35	15.7	7.47

TABLE 8. Frequency behavior of the antenna realized gain (RHCP and LHCP), for the RHCP DRA-based antenna.

f (GHz)	RHCP Gain Without Lens (dBi)	LHCP Gain Without Lens (dBi)	RHCP Gain 7-Disks Lens ($\varepsilon_r = 10.2$) (dBi)	LHCP Gain 7-Disks Lens ($\varepsilon_r = 10.2$) (dBi)	RHCP Gain Massive Lens ($\varepsilon_r = 4$) (dBi)	LHCP Gain Massive Lens ($\varepsilon_r = 4$) (dBi)
5	9.33	-7.5	11.2	-9.5	12.2	-7.39
6	9.94	-3.3	12.2	-8.63	14.2	3.37
7	9.28	-4.51	14.2	-7.8	15.7	3.6
8	9.62	-2.9	14.0	-10.2	15.0	2.08
9	11.1	-5.74	13.5	-3.3	13.6	3.59

as they exhibit efficient, wideband field coupling. This remarkable behavior characterizes massive spherical-axicon lenses, among other structures [1]. Hence, in this section, the focusing characteristics of the proposed petal-shaped and stacked-disk dielectric lenses, when illuminated by an x-polarized uniform incident plane-wave traveling along the lens axis (z-axis) featuring 1V/m amplitude, are gauged vis-a-vis with those of the corresponding benchmark massive

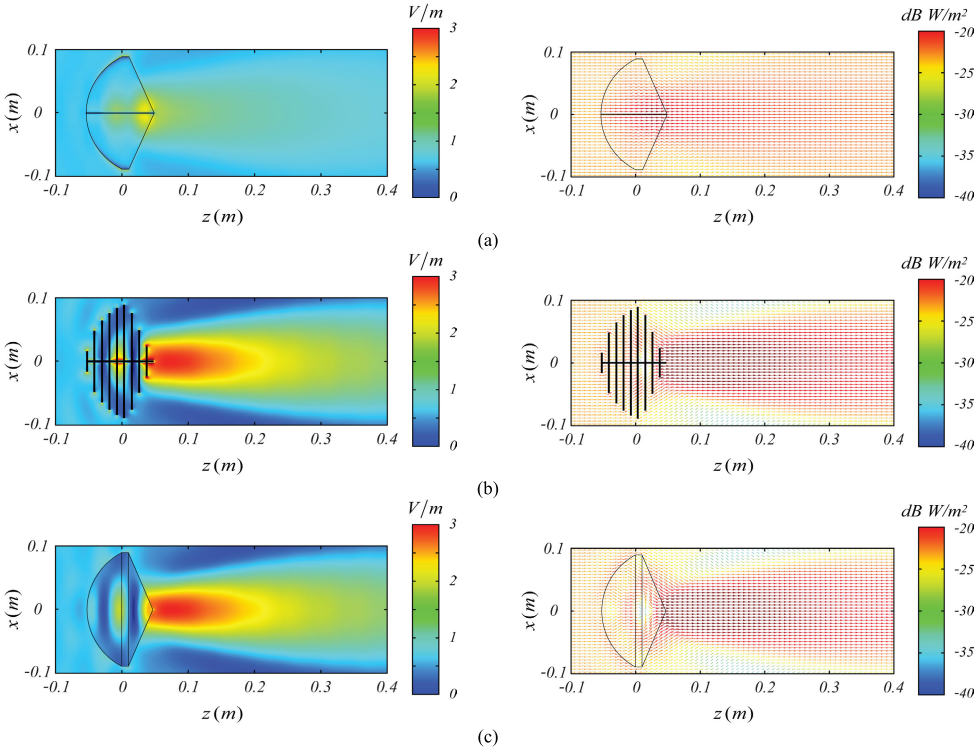

FIGURE 19. Spatial behavior of the x-component of the electric field and of the real part of the Poynting vector in the xz-plane for (a) 8-petal lens; (b) 9-disk lens, both of permittivity $\varepsilon_r = 10.2$; and (c) massive spherical-axicon dielectric lens ($\varepsilon_r = 2.1$), excited by an x-polarized uniform plane wave of amplitude 1 V/m and frequency f = 3 GHz ($D_{lens}/\lambda_0 = 1.78$), traveling along the z-axis. The 9-disk lens focusing performance approaches the massive lens, while the petal-shaped lens performance is inferior.

lens. For the sake of brevity, since the proposed lenses display similar behaviors irrespective of whether they are integrated in Vivaldi or DRA antenna systems, only the former are presented. Because the focusing effectiveness of the proposed lightweight lenses eventually degrades with frequency, whereas the massive lens concurrently assumes an optical behavior, such an analysis is performed in the operating band between 3 GHz (D_{lens}/λ_0 =1.78) and 7 GHz (D_{lens}/λ_0 =4.15).

In Figs. 19-22 the amplitude maps of the x-polarized electric field and the vector plots of the Poynting vector real part in the xz-plane, obtained through the full-wave FIT technique, are shown. The plots illustrate the physical mechanism underpinning the focusing process, which relies on the lens establishing multiple field paths with corresponding phase delays. In particular, in the petal-shaped lens these paths are enabled by surface waves, while in the stacked-disk dielectric lens they are related to refractive and diffractive processes caused by the periodical disk arrangement. As shown in the figures, such distinct mechanisms yield quite differing performances, whereby the 9-disk lens features almost equivalent performances to the massive lens up to about 6 GHz, while the petal-shaped lens performances remain substantially inferior across the operating band.

In the frequency range 3-6 GHz, the petal-shaped lens exhibits a consistently weaker peak field in the focus region (ranging from 1.6 V/m to 2.5 V/m, i.e. 3.9 dB increase) than the stacked-disk dielectric lens (ranging from 2.6 V/m to 4.4 V/m, i.e. 4.6 dB increase). Finally, above 7 GHz the performance of both lightweight lenses degrade rapidly, while the massive lens transitions towards the optical behavior as indicated in Table 9, reaching 13 V/m peak field at 20 GHz (D_{lens}/λ_0 =11.86). Particularly interesting is the field behavior in the stacked-disk lens stop band, highlighted in Fig. 22 at 9 GHz, illustrating how the Poynting vector flips direction inside the 9-disk lens. These behaviors are confirmed by the realized gain behavior versus frequency (see Fig. 11). Table 9 also shows the behavior of the Back Focal Distance (BFD), i.e. the distance from the lens cone vertex to the field peak, and the corresponding field amplitudes, for the considered lenses, in the range 1-20 GHz.

The data summarized in Table 9 describes how the three structures behave in the transition from non-optical to quasi-optical focusing behavior. The petal-shaped lens exhibits an abrupt focus shift away from the cone vertex between 9 GHz and 13 GHz, then a steady reversal at higher frequencies. Instead, the 9-disk lens closely approaches performances similar to those of the massive lens up to about 7 GHz where the field level in the focus region reaches about 4.3 V/m, but then transitions into its first stop-band becoming reflective (see Fig. 22), later re-emerging in a second pass-band between 14 and 19 GHz. Sharp filtering characteristic could

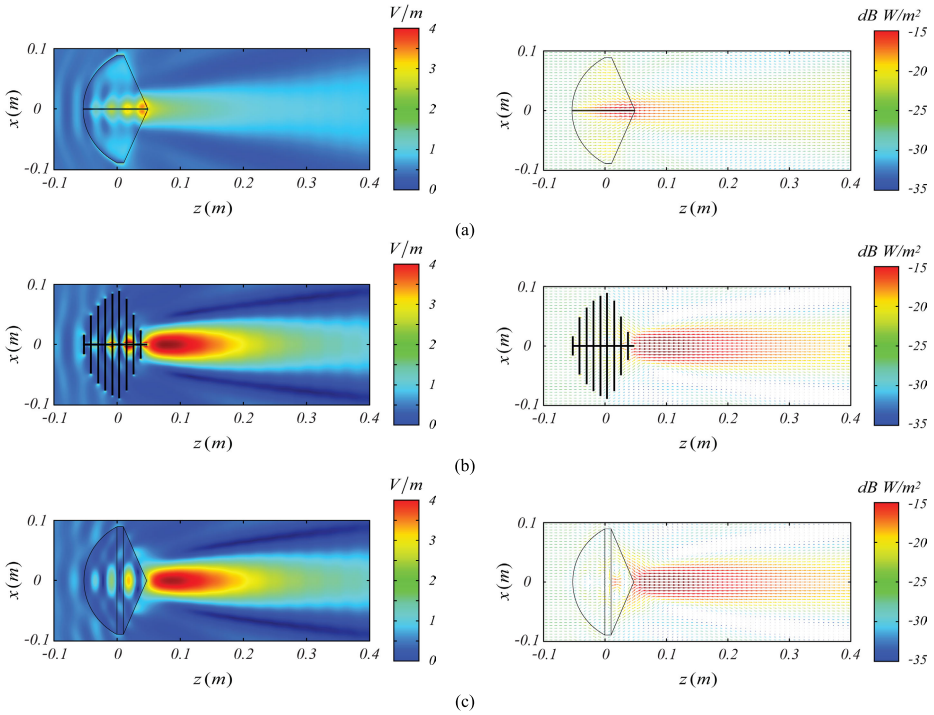

FIGURE 20. Spatial behavior of the x-component of the electric field and of the real part of the Poynting vector in the xz-plane for (a) 8-petal lens; (b) 9-disk lens, both of permittivity $\varepsilon_r = 10.2$; and (c) massive spherical-axicon dielectric lens ($\varepsilon_r = 2.1$), excited by an x-polarized uniform plane wave of amplitude 1 V/m and frequency f = 5 GHz (D_{lens}/λ_0 =2.97), traveling along the z-axis. The 9-disk lens focusing performance approaches the massive lens, while the petal-shaped lens performance remains inferior.

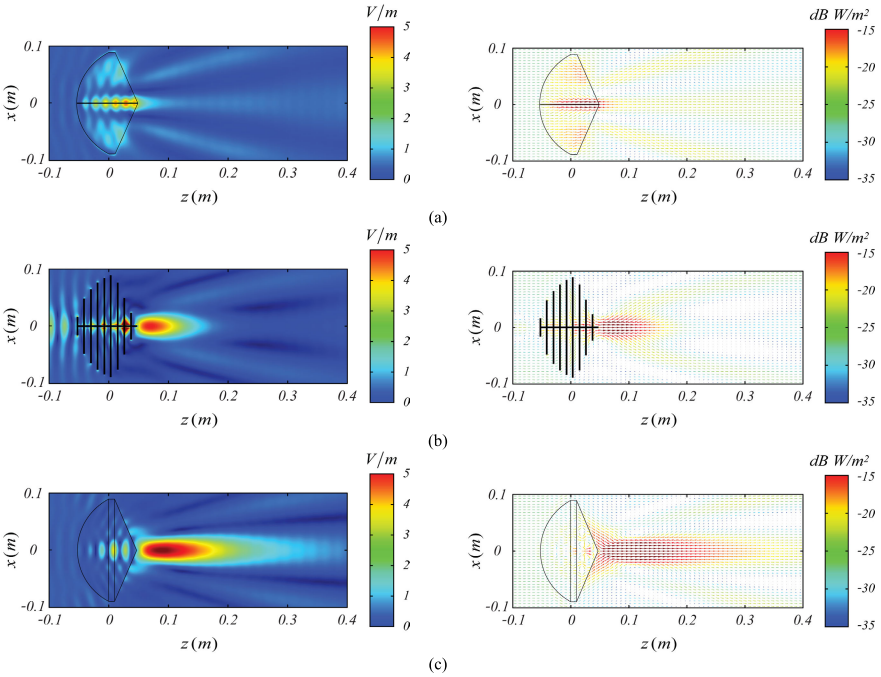

FIGURE 21. Spatial behavior of the x-component of the electric field and of the real part of the Poynting vector in the xz-plane for (a) 8-petal lens; (b) 9-disk lens, both of permittivity $\varepsilon_r = 10.2$; and (c) massive spherical-axicon dielectric lens ($\varepsilon_r = 2.1$), excited by an x-polarized uniform plane wave of amplitude 1 V/m and frequency f = 7 GHz (D_{lens}/λ_0 =4.15), traveling along the z-axis. The 9-disk lens focusing performance begins to depart from the massive lens, while the petal-shaped lens performance is still quite inferior.

be exploited in high-gain radiating system to effect frequency selectivity directly within stacked-disk lenses. A very distinct electromagnetic behavior is observed for the massive lens, featuring substantially stable BFD and steadily increasing peak field versus frequency, thus affirming its performance edge.

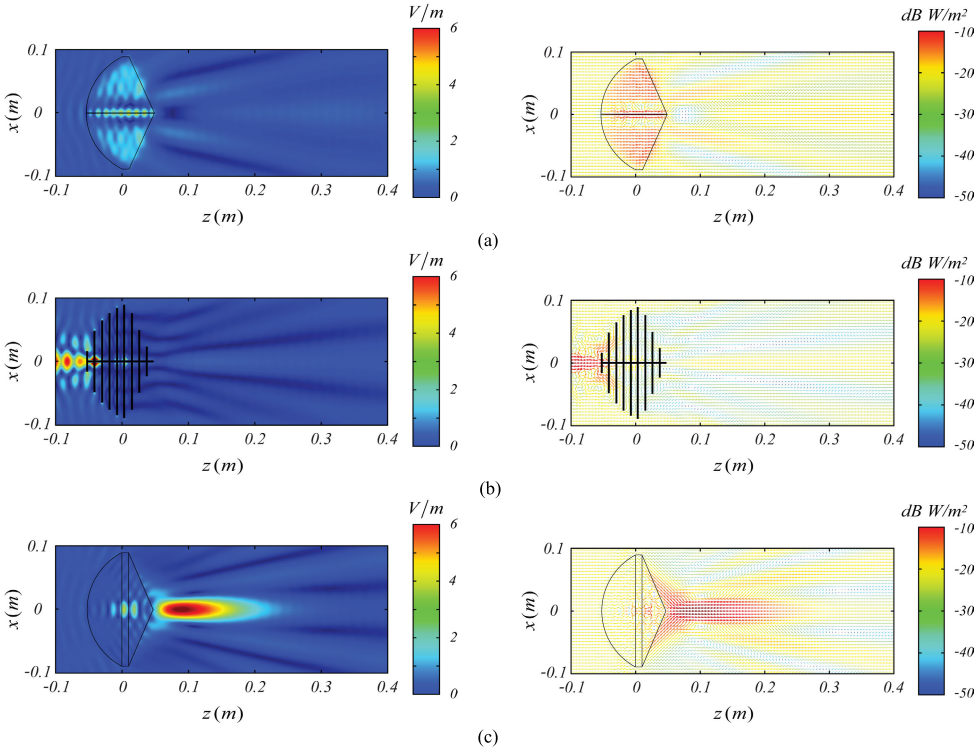

FIGURE 22. Spatial behavior of the x-component of the electric field and of the real part of the Poynting vector in the xz-plane for (a) 8-petal lens; (b) 9-disk lens, both of permittivity $\varepsilon_r = 10.2$; and (c) massive spherical-axicon dielectric lens ($\varepsilon_r = 2.1$), excited by an x-polarized uniform plane wave of amplitude 1 V/m and frequency f = 9 GHz (D_{lens}/λ_0 =5.34), traveling along the z-axis. At this frequency both lightweight lenses lose their focusing properties, and the stop-band behavior of the stacked-disk lens makes it highly reflective. This effect is accompained by the presence of energy vortices both in the internal and in the frontal region of the lens.

IV. LENS DESIGN GUIDELINES

Useful design guidelines are illustrated in the following, featuring two possible approaches, both involving the preliminary optimization of a reference spherical-axicon massive lens.

A. PRELIMINARY MASSIVE LENS OPTIMIZATION

As for plano-covex lenses [1], [21], [27], the attainable gain of spherical-axicon lenses grows with D_{lens}/λ_0, where target antenna size and practical constraints typically dictate the upper bound of D_{lens}. The lens spherical cap radius R_{lens}, its opening angle ϕ_{lens} and the dielectric lens permittivity $\varepsilon_{r_{lens}}$ are then set taking into account that the focal field distance increases with both R_{lens} and ϕ_{lens}, the opposite occurring for higher $\varepsilon_{r_{lens}}$. Undesirable lens resonances may occur as $\varepsilon_{r_{lens}}$ increases [21]; because these resonances as well as the strong lens coupling with the antenna feeding system are not treatable analytically, full-wave simulations are ultimately required at the final optimization stages. The optimized massive lens geometrical envelope is then used to size the corresponding lightweight (petal-shaped or stacked-disk lens) antennas.

While petal-shaped lenses synthesis proceeds by trial and error for the petals thickness and permittivity, the synthesis of stacked-disk lenses takes advantage of Eqs. (5)-(6) to arrive at a preliminary sizing of the disks, thus the latter will be further addressed in the following for the cases of custom or commercial slabs (in both cases, the number of disks N_{disk} stems from the ratio of lens length and cell length l).

B. CUSTOM DIELECTRIC SLAB THICKNESS

Freedom in the choice of the disk thickness t allows combining Eq. (5) with the quasi-static term in Eq. (6), thus expressing t, as well as the elemental cell length l, in terms of the chosen substrate permittivity ε_r, the corresponding quasi-static equivalent permittivity $\varepsilon_{r_{eff}}$, and the desired stop-band frequency f_c, yielding the following design equations

$$l = \frac{2+\pi}{2\pi f_c} \frac{c}{\varepsilon_{r_{eff}}+1} \tag{8}$$

$$t = \frac{2+\pi}{2\pi f_c} \frac{c}{\varepsilon_r - 1} \left(\frac{\varepsilon_{r_{eff}} - 1}{\varepsilon_{r_{eff}} + 1} \right), \tag{9}$$

under the following constraint

$$\varepsilon_r > 1 + \frac{2}{\sqrt{1 + \frac{4}{(2+\pi)^2} \left(\frac{\varepsilon_{r_{eff}}+1}{\varepsilon_{r_{eff}}-1} \right)^2} - 1}. \tag{10}$$

TABLE 9. Lens focus characteristics.

	8 -Petal Dielectric Lens ($\varepsilon_r = 10.2$)		9-Stacked-Disk Dielectric Lens ($\varepsilon_r = 10.2$)		Massive Lens ($\varepsilon_r = 2.1$)	
f (GHz)	Back Focal Distance (cm)	E-Field (V/m)	Back Focal Distance (cm)	E-Field (V/m)	Back Focal Distance (cm)	E-Field (V/m)
1	3.76	1.04	4.67	1.2	3.67	1.22
2	1.32	1.26	1.99	1.84	2.02	1.88
3	0.96	1.58	2.88	2.54	2.76	2.56
4	0.62	1.97	3.32	3.23	3.37	3.23
5	0.47	2.34	3.03	3.95	3.52	3.87
6	0.32	2.56	2.73	4.36	4.11	4.51
7	0.32	2.52	2.14	4.34	3.96	5.09
8	0.17	2.14	-	-	4.11	5.63
9	0.17	1.45	-	-	4.11	6.20
10	8.54	1.37	-	-	3.96	6.78
11	6.3	1.93	-	-	4.26	7.41
12	6.6	2.03	-	-	4.11	8.13
13	6.75	1.85	-	-	3.96	8.87
14	3.91	1.97	22.89	2.63	4.11	9.66
15	3.17	2.63	13.18	4.32	3.96	10.52
16	3.31	1.77	10.2	5.31	3.82	11.26
17	2.12	1.95	7.80	6.26	3.67	11.81
18	1.97	2.47	5.42	6.38	3.67	12.23
19	1.07	1.69	5.87	3.00	3.67	12.64
20	1.52	2.14	1.85	1.93	3.67	13.07

C. COMMERCIALLY-AVAILABLE DIELECTRIC SLAB THICKNESS

Commercially available substrates come with a set of predefined thicknesses. For each available thickness and permittivity, Eqs. (5) and (6) yield l and f_c, as follows

$$l = \frac{\varepsilon_r - 1}{\varepsilon_{r_{eff}} - 1}\, t \tag{11}$$

$$f_c \cong \frac{(2+\pi)c}{2\pi t\,(\varepsilon_r - 1)} \frac{\varepsilon_{r_{eff}} - 1}{\varepsilon_{r_{eff}} + 1}. \tag{12}$$

Finally, observe that choosing $\varepsilon_{r_{eff}} = \varepsilon_{r_{lens}}$ yields a unique set of lens parameters.

V. CONCLUSION

A class of lightweight spherical-axicon-like dielectric lenses for high gain wideband antennas has been presented. The proposed lenses are formed by thin shaped dielectric slabs, either arranged equiangularly (petal-shaped lenses), or stacked orthogonally along the lens axis (stacked-disk lens), so as to follow the geometrical envelope of a benchmark massive spherical-axicon dielectric lens. Two different physical mechanisms governing field propagation and focusing in the aforementioned structures were identified and discussed. Petal-shaped lenses are simple to manufacture and integrate with antenna systems, yielding peak gain increases of the order of just 4 dB in the 3-7 GHz frequency range. Within the same frequency range, stacked-disk dielectric lenses, albeit slightly more complex to assemble, attain performances approaching those of highly effective massive spherical-axicon dielectric lenses, but present sharp stop- and pass-band behaviors due to the spatial periodicity along the lens axis. Approximated formulas expressing the first stop-band onset frequency, as well as the equivalent dielectric permittivity of the stacked-disk lens, have been presented together with useful lens design guidelines. The proposed lenses were analyzed alone in terms of field focusing characteristics, as well as integrated into wideband antennas to outline gain increase and time-domain performances. At least 50% lighter antennas were obtained using stacked-disk lenses mounted on a DRA, while better than 80% weight reduction was achieved when the same lens is integrated in a Vivaldi antenna system. Both the proposed lightweight dielectric lenses provide excellent time-domain performances, comparable with

the massive lens. Consequently, they represent attractive, lightweight alternatives to massive spherical-axicon lenses for broadband antennas, providing high gain and improved front-to-back ratio when operating with time-harmonic or impulsive signals.

REFERENCES

[1] J. Thornton and K.-C. Huang, *Modern Lens Antennas for Communications Engineering*. Hoboken, NJ, USA: Wiley, 2013.
[2] J. Ala-Laurinaho, J. Aurinsalo, A. Karttunen, M. Kaunisto, A. Lamminen, J. Nurmiharju, A. V. Räisänen, J. Säily, and P. Wainio, "2-D beam-steerable integrated lens antenna system for 5G E-band access and backhaul," *IEEE Trans. Microw. Theory Techn.*, vol. 64, no. 7, pp. 2244–2255, Jul. 2016.
[3] B. T. Malik, V. Doychinov, S. A. R. Zaidi, I. D. Robertson, and N. Somjit, "Antenna gain enhancement by using low-infill 3D-printed dielectric lens antennas," *IEEE Access*, vol. 7, pp. 102467–102476, 2019.
[4] R. B. D. Silveira and A. R. Holt, "An automatic identification of clutter and anomalous propagation in polarization-diversity weather radar data using neural networks," *IEEE Trans. Geosci. Remote Sens.*, vol. 39, no. 8, pp. 1777–1788, Aug. 2001.
[5] W. Menzel and A. Moebius, "Antenna concepts for millimeter-wave automotive radar sensors," *Proc. IEEE*, vol. 100, no. 7, pp. 2372–2379, Jul. 2012.
[6] A. Vorobyov, J. R. Farserotu, and J.-D. Decotignie, "3D printed antennas for mm-wave sensing applications," in *Proc. 11th Int. Symp. Med. Inf. Commun. Technol. (ISMICT)*, Lisbon, Portugal, Feb. 2017, pp. 23–26.
[7] K. Mu, T. H. Luan, L. Zhu, L. X. Cai, and L. Gao, "A survey of handy see-through wall technology," *IEEE Access*, vol. 8, pp. 82951–82971, 2020.
[8] R. Cicchetti, V. Cicchetti, S. Costanzo, P. D'Atanasio, A. Fedeli, M. Pastorino, S. Pisa, E. Pittella, E. Piuzzi, C. Ponti, A. Randazzo, M. Santarsiero, G. Schettini, and O. Testa, "A microwave imaging system for the detection of targets hidden behind dielectric walls," in *Proc. 33rd URSI GASS*, Rome, Italy, Aug. 2020, pp. 1–4.
[9] R. Cicchetti, S. Pisa, E. Piuzzi, E. Pittella, P. D'Atanasio, and O. Testa, "Numerical and experimental comparison among a new hybrid FT-music technique and existing algorithms for through-the-wall radar imaging," *IEEE Trans. Microw. Theory Techn.*, vol. 69, no. 7, pp. 3372–3387, Jul. 2021.
[10] A. Jernberg, M. Pinkasy, G. Pinchuk, T. Haze, R. Konevky, L. Shmidov, R. Braun, B. Gershkovich, G. Baran, P. Iversen, A. Giacomini, L. J. Foged, F. Saccardi, and M. Boumans, "Short focal length compact antenna test range for large L/Ku-band antenna measurements," in *Proc. IEEE Indian Conf. Antennas Propogation (InCAP)*, Dec. 2018, pp. 1–3.
[11] E. Woerner, C. Wild, W. Mueller-Sebert, and P. Koidl, "CVD-diamond optical lenses," *Diamond Rel. Mater.*, vol. 10, nos. 3–7, pp. 557–560, Mar. 2001.
[12] C. A. Fernandes, J. R. Costa, E. B. Lima, and M. G. Silveirinha, "Review of 20 years of research on microwave and millimeter-wave lenses at instituto de telecomunicações," *IEEE Antennas Propag. Mag.*, vol. 57, no. 1, pp. 249–268, Feb. 2015.
[13] X. Wu, G. V. Eleftheriades, and T. E. V. Deventer-Perkins, "Design and characterization of single- and multiple-beam mm-wave circularly polarized substrate lens antennas for wireless communications," *IEEE Trans. Microw. Theory Techn.*, vol. 49, no. 3, pp. 431–441, Mar. 2001.
[14] C. A. Fernandes, E. B. Lima, and J. R. Costa, *Dielectric Lens Antennas: Handbook of Antenna Technologies*. New York, NY, USA: Springer, 2015.
[15] G. H. Lee, S. Kumar, H. C. Choi, and K. W. Kim, "Wideband high-gain double-sided dielectric lens integrated with a dual-bowtie antenna," *IEEE Antennas Wireless Propag. Lett.*, vol. 20, no. 3, pp. 293–297, Mar. 2021.
[16] Y. He, Y. Chen, L. Zhang, S.-W. Wong, and Z. N. Chen, "An overview of terahertz antennas," *China Commun.*, vol. 17, no. 7, pp. 124–165, Jul. 2020, doi: 10.23919/J.CC.2020.07.011.
[17] R. Cicchetti, V. Cicchetti, A. Faraone, L. Foged, and O. Testa, "A compact high-gain wideband lens Vivaldi antenna for wireless communications and through-the-wall imaging," *IEEE Trans. Antennas Propag.*, vol. 69, no. 6, pp. 3177–3192, Jun. 2021.
[18] L. B. Felsen and N. Marcuvitz, *Radiation and Scattering of Waves*. New York, NY, USA: Prentice-Hall, 1994.
[19] K. Phaebua, N. Chudpooti, S. Kittiwittayapong, T. Lertwiriyaprapa, D. Torrungrueng, and H.-T. Chou, "One-sixteenth spherical homogeneous dielectric lens antenna using partially reflective surface for size reduction and high-gain radiation," *IEEE Antennas Wireless Propag. Lett.*, vol. 20, no. 2, pp. 184–188, Feb. 2021.
[20] K. Liu, C. Zhao, S.-W. Qu, Y. Chen, J. Hu, and S. Yang, "A 3-D-printed multibeam spherical lens antenna with ultrawide-angle coverage," *IEEE Antennas Wireless Propag. Lett.*, vol. 20, no. 3, pp. 411–415, Mar. 2021.
[21] R. A. dos Santos, G. L. Fré, and D. H. Spadoti, "Technique for constructing hemispherical dielectric lens antennas," *Microw. Opt. Technol. Lett.*, vol. 61, no. 5, pp. 1349–1357, May 2019.
[22] O. Yurduseven, D. Cavallo, and A. Neto, "Wideband dielectric lens antenna with stable radiation patterns fed by coherent array of connected leaky slots," *IEEE Trans. Antennas Propag.*, vol. 62, no. 4, pp. 1895–1902, Apr. 2014.
[23] D. Isakov, C. J. Stevens, F. Castles, and P. S. Grant, "3D-printed high dielectric contrast gradient index flat lens for a directive antenna with reduced dimensions," *Adv. Mater. Technol.*, vol. 1, no. 6, Sep. 2016, Art. no. 1600072.
[24] H. Xin and M. Liang, "3-D-printed microwave and THz devices using polymer jetting techniques," *Proc. IEEE*, vol. 105, no. 4, pp. 737–755, Apr. 2017.
[25] M. A. Belen and P. Mahouti, "Design of nonuniform substrate dielectric lens antennas using 3D printing technology," *Microw. Opt. Technol. Lett.*, vol. 62, no. 2, pp. 756–762, Feb. 2020.
[26] M. S. Anwar, H. Abufanas, and A. Bangert, "3D printed dielectric lens for the gain enhancement of a broadband antenna," *Int. J. RF Microw. Comput.-Aided Eng.*, vol. 30, no. 4, pp. 1–7, Apr. 2020.
[27] K. K. Sharma, *Optics: Principles and Applications*. Cambridge, MA, USA: Academic, 2006.
[28] Y. Wang, S. Yan, A. T. Friberg, D. Kuebel, and T. D. Visser, "Electromagnetic diffraction theory of refractive axicon lenses," *J. Opt. Soc. Amer. A, Opt. Image Sci.*, vol. 34, no. 7, pp. 1201–1211, Jul. 2017.
[29] R. Cicchetti, A. Faraone, E. Miozzi, R. Ravanelli, and O. Testa, "A high-gain mushroom-shaped dielectric resonator antenna for wideband wireless applications," *IEEE Trans. Antennas Propag.*, vol. 64, no. 7, pp. 2848–2861, Jul. 2016.
[30] M. Manteghi and Y. Rahmat-Samii, "Multiport characteristics of a wideband cavity backed annular patch antenna for multipolarization operations," *IEEE Trans. Antennas Propag.*, vol. 53, no. 1, pp. 466–474, Jan. 2005.
[31] R. Cicchetti, A. Faraone, and O. Testa, "Energy-based representation of multiport circuits and antennas suitable for near- and far-field syntheses," *IEEE Trans. Antennas Propag.*, vol. 67, no. 1, pp. 85–98, Jan. 2019.
[32] Z. N. Chen, X. H. Wu, H. F. Li, N. Yang, and M. Y. W. Chia, "Considerations for source pulses and antennas in UWB radio systems," *IEEE Trans. Antennas Propag.*, vol. 52, no. 7, pp. 1739–1748, Jul. 2004.
[33] P. K. Kumar and T. K. Kumar, "UWB impulse radar for through-the-wall imaging," *Int. J. Electromagn. Appl.*, vol. 1, no. 1, pp. 19–23, Aug. 2012, doi: 10.5923/j.ijea.20110101.05.
[34] C. Ponti, M. Santarsiero, and G. Schettini, "Electromagnetic scattering of a pulsed signal by conducting cylindrical targets embedded in a half-space medium," *IEEE Trans. Antennas Propag.*, vol. 65, no. 6, pp. 3073–3083, Jun. 2017.
[35] R. Collin, *Field Theory of Guided Waves*, 2nd ed. New York, NY, USA: IEEE Press, 1991.

RENATO CICCHETTI (Senior Member, IEEE) was born in Rieti, Italy, in May 1957. He received the Laurea degree *(summa cum laude)* in electronics engineering from the University of Rome "La Sapienza," Rome, Italy, in 1983. From1983 to 1986, he was an Antenna Designer at Selenia Spazio S.p.A. (now Thales Alenia Space S.p.A.), Rome, where he was involved in studies on theoretical and practical aspects of antennas for space application and scattering problems. From 1986 to 1994, he was a Researcher, and from 1994 to 1998, he was an Assistant Professor at the Department of Electronics Engineering, University of Rome "La Sapienza," where he is currently a Full Professor. In 1998, 2002, and 2006, he was Visiting Professor at the Motorola Florida Corporate Electromagnetics Research Laboratory, Fort Lauderdale, FL, USA, where he was involved with antennas for cellular and wireless communications.

His current research interests include electromagnetic field theory, asymptotic techniques, electromagnetic compatibility, wireless communications, microwave and millimeter-wave integrated circuits, and antennas. He is a Member of the Italian Electromagnetic Society (SIEm). His results listed in Marquis Who's Who in the World and Who's Who in Science and Engineering. Since 2012, he has been the Lead Editor of the Annual Special Issue on "Wideband, Multiband, Tunable, and Smart Antenna Systems for Mobile and UWB Wireless Applications" for the *International Journal of Antennas and Propagation.* Finally, from 2016 until mid-2019 he was one of the coordinators of the research project "Ultra-wideband Virtual Imaging Extra Wall for High-Penetration High Quality Imagery of Enclosed Structures" (U-VIEW) funded by the Italian Ministry of Education, University and Research (MIUR).

VALENTINA CICCHETTI was born in Isernia, Italy, in 1993. She received the master's degree *(cum laude)* in electronics engineering from the Sapienza University of Rome, in 2018, where she is currently pursuing the Ph.D. degree in information and communications technology. Her research interests include applied electromagnetics, wide-band and ultrawide-band antenna systems, and the analysis of the related electromagnetic compatibility problems.

ANTONIO FARAONE (Senior Member, IEEE) was born in Rome, Italy, in 1966. He received the Ph.D. degree in applied electromagnetics from the University of Rome "La Sapienza," in 1997. He joined Motorola (now Motorola Solutions Inc.) Corporate Electromagnetic Energy (EME) Research Laboratory, Fort Lauderdale, FL, USA, engaging in mobile antenna technology and RF dosimetry research, as well as the IEEE and IECRF exposure safety and product compliance standards. At Motorola Solutions, he serves as the Chief EME Scientist, over-seeing product RF exposure compliance, where he is a Scientific Advisory Board Associates (SABA) Member, a Master Innovator, and a Dan Noble Fellow. He has coauthored 37 refereed journal publications and holds 39 patents, mostly on antenna technologies. He currently holds the Chair of the Board of Directors of the Mobile & Wireless Forum, an international industry association supporting research into RF health and safety and promoting wireless device integrity and accessibility.

ORLANDINO TESTA received the Laurea degree *(cum laude)* in electronic engineering and the Ph.D. degree from the University of Rome "La Sapienza," Rome, Italy, in 1997 and 2003, respectively. Since 2001, he has been a High School Teacher with the ITIS "G. Armellini" Institute of Rome, Rome, where he is involved in teaching electronics and telecommunications. He is currently collaborating with the Department of Electronic Engineering, University of Rome "La Sapienza." At present, he is studying high-frequency models for the analysis of radio coverage in indoor environments and tunnels with particular attention to EMC/EMI problems. His research interests include propagation and radiation of electromagnetic fields, electromagnetic compatibility, microwave and millimeter-wave integrated circuits, and antennas.